ADVANCED ELECTRONIC MATERIALS Open Access
www.advelectronicmat.de

P-type Semiconducting Polymers as Photocathodes: A Comparative Study for Optobioelectronics

*Luca Bondi, Camilla Marzuoli, Edgar Gutiérrez-Fernández, Gabriele Tullii, Jaime Martín, Beatrice Fraboni, David Mecerreyes, Maria Rosa Antognazza, and Tobias Cramer**

Recent studies have shown that p-type polymeric semiconductors enable a new type of wireless, optically triggered interface with cells and tissues. Poly(3-hexylthiophene-2,5-diyl) (P3HT) has already been used to create such optobioelectronic interfaces, producing reactive oxygen species and hydrogen peroxide that act as messengers in biological systems to impact cell signaling and proliferation. However, the use of P3HT in biomedical in-vivo applications is limited as its optical absorption does not match the tissue transparency window. This paper compares the performance of P3HT with two low band-gap polymers commonly employed in high-performance organic solar cells, namely Poly[[4,8-bis[5-(2-ethylhexyl)-2-thienyl]benzo[1,2-b:4,5-b′]dithiophene-2,6-diyl]-2,5-thiophenediyl[5,7-bis(2-ethylhexyl)-4,8-dioxo-4H,8H-benzo[1,2-c:4,5-c′]dithiophene-1,3-diyl]] (PBDB-T) and Poly({4,8-bis[(2-ethylhexyl)oxy]benzo[1,2-b:4,5-b′]dithiophene-2,6-diyl}{3-fluoro-2-[(2-ethylhexyl)carbonyl]thieno[3,4-b] thiophenediyl}) (PTB7). Their photogeneration capabilities are quantified in physiological-like conditions through photocurrent analysis and a hydrogen peroxide assay, finding a superior photocurrent generation and a better H_2O_2 photogeneration yield in PTB7 as compared to the other two polymers. Spectroscopic and structural investigations are used to compare such differences by comparing their energy levels at the electrochemical interface and their morphologies. Finally, biocompatibility is tested both in dark and illuminated conditions and effective in-vitro intracellular ROS production is demonstrated. These findings provide insight into the physico-chemical properties crucial for the development of novel, less invasive, optically operated bioelectronic interfaces.

1. Introduction

Organic semiconductors are soliciting strong interest as active materials in novel bioelectronic interfaces. As organic materials they have an enormous chemical versatility and can be designed to meet the multifunctional properties requested for interfaces with living biological cells. Recent literature examples demonstrate how semiconducting charge transfer properties are combined with soft mechanical behavior as well as chemical stability and biocompatibility to improve traditional microelectrode based interfaces for bioelectronic recordings and stimulations.[1–7] On top of that, recent findings show that the outstanding optoelectronic properties of organic semiconductors enable conceptually novel types of optobioelectronic interfaces.[5–9] The aim is to substitute invasive wires and implantable electronics by a single unconnected organic transducer device that is operated by light pulses transmitted through the surrounding tissue. First examples for this concept are organic semiconductor based retinal implants[10–13] or nerve stimulators[14] as well as optically controlled smart surfaces to guide tissue growth and cell regeneration.[15–19] All these applications rely on the transduction of light pulses to physico-chemical stimuli at the semiconductor/electrolyte interface further effecting on biological processes.

L. Bondi, B. Fraboni, T. Cramer
DiFA University of Bologna
Viale Carlo Berti Pichat 6/2, Bologna 40127, Italy
E-mail: tobias.cramer@unibo.it

The ORCID identification number(s) for the author(s) of this article can be found under https://doi.org/10.1002/aelm.202300146

DOI: 10.1002/aelm.202300146

C. Marzuoli, G. Tullii, M. R. Antognazza
Center for Nano Science and Technology
Istituto Italiano di Tecnologia
Via Rubattino 81, Milano 20134, Italy

C. Marzuoli
Politecnico di Milano
Dipartimento di Fisica
Piazza Leonardo da Vinci 32, Milano 20133, Italy

E. Gutiérrez-Fernández, J. Martín, D. Mecerreyes
POLYMAT
Tolosa Hiribidea 76, Donostia-San Sebastian 20018, Spain

E. Gutiérrez-Fernández, J. Martín, D. Mecerreyes
UPV-EHU
Chemistry Department
Paseo Manuel Lardizabal 3, Donostia-San Sebastián 20018, Spain

Accordingly, material science is required to investigate the different light enabled transduction mechanisms and performances that can be achieved in this context with organic semiconductors.

Different architectures of organic optoelectronic interfaces have been presented in the literature such as planar p-n heterojunctions,[10,20–22] polymeric thin films,[12,23] structured polymeric films,[19,24] and polymeric nanoparticles.[25–27] In these architectures, semiconducting polymers offer several advantages compared to other materials such as high optical absorption and multiple photostimulation mechanisms,[21] high biocompatibility, mechanical compliance and synthetic flexibility. As the application requires a direct contact with the aqueous electrolyte containing the biological target, a suitable energetic alignment with the redox species present in water[28,29] is required. P-type organic semiconductors can fulfill this requirement and a high stability toward electrochemical degradation processes has been demonstrated combined with the selective activation of photoelectrochemical processes.

Depending on the architecture and the materials, different optically excited transduction mechanisms impacting on adjacent cell have been established. Thermal activation aims at a significant increase in temperature close to the illumination site. Due to the high thermal transport properties of water, significant localized increases of temperature are only achieved with high light intensities (>>100 mW cm^{-2}).[30] At lower light intensities, electrochemical phototransduction mechanisms play a key role in the modulation of cellular physiology. They can be divided into two main categories: i) Photocapacitive and ii) photofaradaic mechanisms. Photocapacitive stimulation occurs when the semiconducting layer builds-up a photovoltage upon illumination.[20] The photovoltage drives an ionic displacement current that charges the Debye-Helmholtz capacitance at the semiconductor's interface. The transient displacement current affects cells adhering to the surface similar to current injecting stimulation electrodes.[22] Consequently light pulses can be transduced into cell membrane depolarization triggering action potentials in excitable tissue. Heterojunctions of p- and n-type organic semiconductors or metal/semiconductor interfaces have been exploited to maximize photovoltage generation. The first example demonstrating this concept is the bulk heterojunction developed by the Lanzani group[31] which consist of a binary polymeric blend made of the poly-3-Hexylthiophene (P3HT) polymer and [6,6]-Phenyl-C61-butyric acid methyl ester (PCBM). A highly stable junction for photocapacitive stimulations is made by the organic pigments H2PC-PTCDI thin-film molecular planar heterojunction developed by Glowacki and coworkers.[10,21] It has been demonstrated that also a single layer of p-type polymer such as P3HT can build-up photovoltage due to photoelectrochemical reactions.[29,32] This simplification has important implications, as it can be applied to p-type semiconducting nanoparticles interacting directly with the cell membrane to stimulate cells, even though the operating mechanism is still under debate.[25,33]

A second relevant pathway to stimulate cells relies on semiconductor photo-electrochemistry. Here excited charge carriers transfer through the semiconductor/water interface and cause oxidation or reduction reactions in the biological system. Such photofaradaic processes have to be tuned to generate electrochemical messenger molecules that impact on cellular processes.[8] We note that an organic semiconductor device in direct contact with the aqueous electrolyte can follow both stimulation mechanisms, photocapacitive as well as photofaradaic.[21] One process can prevail over the other, depending on the semiconductor energy levels and their alignment with redox species as well as kinetic barriers for electron transfer. Both processes start under illumination by the generation of localized excitons and their subsequent dissociation into free carriers occurring at interfacial electric fields or spontaneously.[34] In the capacitive case, the free carriers accumulate and modulate the space charge in the device also affecting the Debye Helmholtz layer and generating ionic displacement currents. In photofaradaic reactions, free electrons in the conduction band are transferred to acceptor states in solution or alternatively hole carriers in the valence band oxidize donors in solution. Photofaradaic or photocapacitive processes can be easily distinguished through chronoamperometric measurements in dark-light-dark conditions: the integral of a cycle amounts to the overall photofaradaic current; the photocapacitive contribution is then the total current minus the photofaradaic one.[21]

In the case of p-type polymers, such as P3HT or poly(3,4-ethylenedioxythiophene) (PEDOT), the typical acceptor molecule taking free electrons is oxygen, always present in biological conditions.[32,35,36] The oxygen reduction reaction (ORR) generates H_2O_2 on organic semiconductor surfaces and other intermediate ROS species.[37,38] Importantly, the ORR products are known to act as messenger substances with impact on cell homeostasis, cell metabolism and regenerative processes. The photofaradaic generation of ROS species has been employed through the use of organic semiconductor thin films as well as injectable nanoparticles and was demonstrated to be effective in stimulating cell regeneration.[13,23,31,39,40] The detailed mechanism of the photofaradaic transduction chain depends on the physicochemical interactions occurring at the interface with the cellular medium[8,21] and between the ROS and the particular cell line.[41] Steady state physiological flux of H_2O_2 to specific protein targets leads to reversible oxidation, altering protein activity, localization and interactions.[42] This contributes to adaptation of various processes in cells and organs, including cell proliferation, differentiation, migration and angiogenesis.[43,44] Overall, physiological targets of ROS serve as redox switches in signal transduction acting in response to stressors or external perturbations.[42]

Most of the studies were conducted on single-polymer photoelectrodes and relied on the use of regioregular P3HT (rr-P3HT), characterized by a semicrystalline structure, low glass transition temperature ($T_g \approx T_{amb}$) and a noticeable chain mobility.[45] This material has recently been under the spotlight as an effective photocathode for triggering cell differentiation pathways through the production of Reactive Oxygen Species (ROS),[25,28] nevertheless it has some weak spots in perspective of clinical implementation. For instance, its absorption spectrum (c.a. 450–650 nm) does not match the therapeutical window (650-1350 nm). In this context, the introduction of novel materials and the study of how they interface with the biological medium is important to overcome current limitations and to improve the desired photoelectrochemical behavior. From OPV research similar p-type semiconducting polymer materials are known which feature high performances and lower bandgaps, such as Poly [[4,8-bis[(2-ethylhexyl)oxy]benzo[1,2-b:4,5-b']dithiophene-2,6-diyl][3-fluoro-2-[(2-ethylhexyl)carbonyl]thieno[3,4-b]thiophenediyl]] (PTB7),

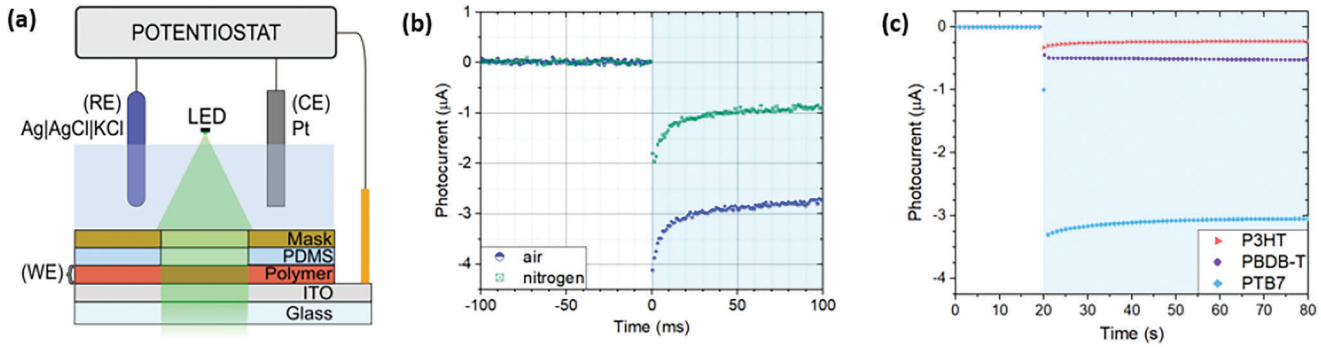

Figure 1. Photofaradaic transients produced by p-type organic semiconductor photoelectrodes. a) Scheme of the photoelectrochemical cell. b) Comparison between the photocurrent transients of a 50 nm P3HT thin-film illuminated with a 20 mW cm^{-2} 470 nm LED in presence of ambient air and after oxygen removal. c) Comparison of photocurrent transient generated by different p-type organic semiconductor thin films. Light intensity is 110 mW cm^{-2}. LED excitation wavelength matches the polymer absorption peak (530 nm for P3HT and PBDB-T and 660 nm for PTB7). All transients were recorded at open circuit potential as determined in dark and the electrode area was 1cm^2.

poly[(2,6-(4,8-bis(5-(2-ethylhexyl)thiophen-2-yl)-benzo[1,2-b:4,5-b']dithiophene))-alt-(5,5-(1',3'-di-2-thienyl-5',7'-bis(2-ethylhexyl)benzo[1',2'-c:4',5'-c'] dithiophene-4,8-dione)] (PBDB-T). The HOMO levels of these materials are between −4.6 and −5.3 eV[46–49] and the optical bandgap between 1.5 and 2 eV.[50–52] The position of the energy bands relative to donor and acceptor levels at the semiconductor-water interface is of fundamental importance also in determining the stability of the photoelectrode,[32,53] as well as the possible back electron transfer pathways. Among the latter, are worth of mention the polymer reduction by means of ROS species and the oxidation of water by means of positively charged states in the polymer. In addition to energetic aspects, the polymers differ in the processability, the solubility in common solvents, the chemical stability and in structural factors. For example, the structural order can space from totally amorphous to paracrystalline, in regiorandom polymers or polymers with a small number of repetitive units, up to semicrystalline order in regioregular and high molecular weight polymers like rr-P3HT.[54] Moreover, the T_g of all the mentioned OPV materials is much higher than the sub-room temperature T_g of rr-P3HT,[55] implying a lower chain mobility.

The aim of the work is to compare different p-type organic semiconductors for photofaradaic ROS generation at optobioelectronic interfaces, in aqueous environment. Among the possible p-type low-bandgap biocompatible polymeric materials, we chose for our studies 2 materials to compare to P3HT, namely PBDB-T and PTB7, based on their chemical-physical properties. These are low bandgap, highly absorbing polymers[56] with high photoconversion yield well characterized for OPV applications.[57,58] The LUMO level of these materials are compatible with oxygen photoreduction while having a HOMO energy not suitable for efficient water oxidation processes. We perform photoelectrochemical experiments under physiologic conditions to determine both photocurrent generation and H_2O_2 generation efficiencies. Absorption spectra and photocurrent spectra are acquired and combined with Kelvin-Probe force microscopy measurements to determine the energy level diagrams for the electrode/polymer junction. We conclude our physicochemical characterizations of the materials with structural investigations of the photoelectrode thin films by means of AFM and GIWAXS. Finally, we demonstrate the biocompatibility of the materials and their ability to increase intra-cellular ROS formation in–vitro. The systematic comparison allows us to determine relations between physico-chemical properties and photoelectrochemical performances of importance for such novel optoelectronic interfaces.

2. Results and discussion

2.1. Photoelectrochemical Characterization

We characterize the oxygen reduction properties of p-type organic semiconducting polymer thin films P3HT, PTB7 and PBDB-T, prepared by spin coating chlorobenzene solutions onto Indium-Tin-Oxide (ITO)-covered glass slides. Conditions were optimized to obtain a thickness value of ≈50 nm for all polymers. The Photoelectrochemical Cell (PEC) setup used to perform the measurements is introduced in **Figure 1**a. The active area of the photoelectrode in contact with electrolyte (PBS – 137 mM NaCl, 3 mM KCl, 10 mM Phosphate buffer, pH 7.4) is confined by a PDMS O-ring and the same area is illuminated from the electrolyte side. The photoelectrode is connected as the working electrode to a potentiostat. A Pt-wire and an Ag|AgCl|KCl (3 M) electrode are used as counter and reference electrode, respectively. **Figure 2**b shows typical photocurrent transients obtained with the P3HT photoelectrode when measured in ambient air and after oxygen removal by fluxing N_2 for 60 min. Upon illumination a cathodic current is observed; after the initial transient dynamics an equilibrium photocurrent signal is established within tens of millisecond. The absence of oxygen causes a significant reduction in current and confirms the central role of oxygen in the generation of photocurrent in this class of materials. The remaining photocurrent intensity can be attributed to different mechanisms, including H^+ reduction to gaseous H_2.[59]

Figure 1c compares the long-term Faradaic photocurrent obtained with the different semiconductors in aerated electrolytes. Since the absorption spectra of the compared materials are different, two LEDs were chosen to have comparable absorption coefficients, namely 530 nm/2.35 eV for P3HT and PBDB-T and

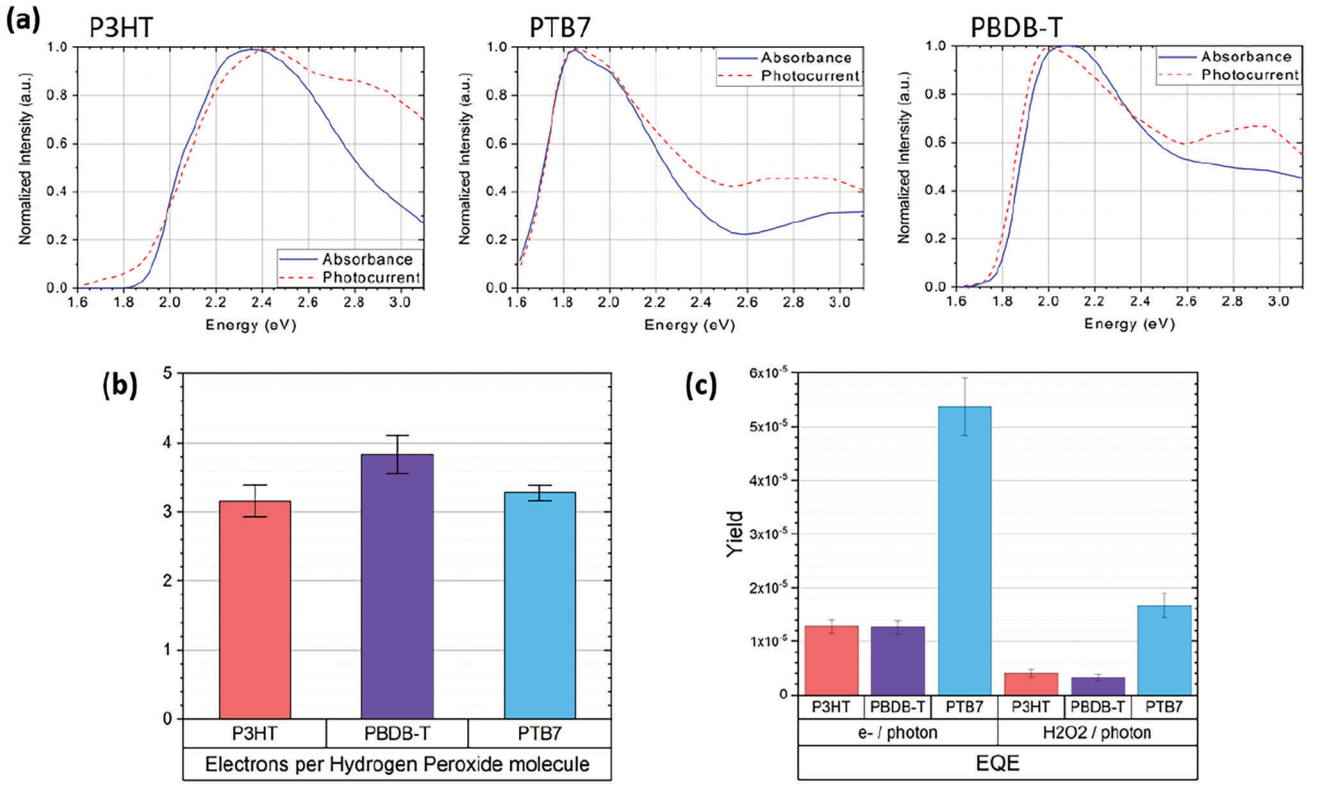

Figure 2. Spectroscopy and efficiency of photocathodic current: a) Normalized absorption and photoelectrochemical current spectra of the three different photoelectrode materials; b) ratio between the net charge passed through the WE and the concentration of H_2O_2 measured in water during 1 h of illumination with a near band-gap LED (530 nm for P3HT and PBDB-T and 660 nm for PTB7) at an irradiance of 110 mW cm^{-2}; c) External Quantum Efficiency (EQE) comparison of the three studied polymers.

Table 1. Data acquired with 50 nm organic semiconductor thin films deposited on ITO photoelectrodes, illuminated area = 1 cm^2, 110 mW cm^{-2} LED light source, PBS electrolyte. Photocurrent (PC) and H_2O_2 generation are measured at the open circuit potential measured in dark conditions (OCP Dark). The hydrogen peroxide generation experiment lasted 60 min. The voltages are referred to Ag|AgCl 3.0 M reference electrode.

	LED wavelength	Absorbance [at LED wavelength]	OCP Dark	Max OCP Illuminated	Photocurrent at OCP dark	H_2O_2 generation EQE [x10^{-6}]
P3HT	530 [nm]	0.24 ± 0.01 [A]	+ 0.12 [V]	+ 0.35 [V]	0.23 [μA]	4.05 ± 0.67
PTB7	660 [nm]	0.37 ± 0.03 [A]	+ 0.17 [V]	+ 0.44 [V]	3.04 [μA]	16.75 ± 2.29
PBDB-T	530 [nm]	0.31 ± 0.02 [A]	+ 0.24 [V]	+ 0.54 [V]	0.54 [μA]	3.31 ± 0.54

660 nm/1.88 eV for PTB7 (see **Table 1**). The biomedical application of such thin films as photoelectrodes is motivated by the wireless operation and hence in absence of ground connection inside the biological tissue. Accordingly, we carried out the photocurrent experiments at open circuit potential (OCP) as determined in dark condition at equilibrium as listed in Table 1. We note that the ungrounded condition, would cause the accumulation of positive charge in the polymer during photocathodic activity and it would slow down further photoconversion. Hence, the photocurrent values measured at OCP dark provide an upper limit for the polymers' performance. In these conditions, PTB7 outperforms the other polymers in photocurrent generation, and exceeds by 5 times the photocurrent per absorbed mW of PBDB-T and ≈10 times the one of P3HT. (Table 1).

Next, we investigate the spectral properties of the photoelectrochemical current and compare with absorption spectroscopy. The first near-infrared window (also known as therapeutic window) defines the range of wavelength where light has its maximum depth of penetration in living tissue, and spans between 625 nm and 1315 nm, which corresponds to energies between 0.95 eV and 2 eV.[60] In this regard, the absorption spectra in Figure 2a identify PTB7 as the most suitable material for in–vivo applications. The PTB7 absorption peak fits perfectly into the transparency window, thus minimizing the energy losses, due to unspecific tissue dispersion, in in–vivo applications. Figure 2a also shows the comparison between absorption and photocurrent spectra. All the materials show a good agreement between the two curves, especially close to the bandgap energy, suggesting that photocurrent is generated through a mechanism based on HOMO-LUMO excitation in the bulk, exciton generation and separation into free carriers and ultimately transfer of free carriers onto electrochemical species. All the materials show an

enhanced photogeneration yield in the supra-bandgap energy probably due to an increased exciton generation rate caused both by optical interference inside the film as well as a higher polaron pair formation efficiency.[61]

A crucial parameter for any targeted biological application is the reduction reaction efficiency.[28] For organic semiconductors, a four-electron reduction process is very unlikely to be efficient and instead the ultimate product of ROS generation is H_2O_2.[35,62]

$$O_2 + e^- \rightarrow O_2^- \quad O_2^- + 2H^+ + e^- \rightarrow H_2O_2 \tag{1}$$

Here, we quantify the amount of generated H_2O_2 in PBS by using the HRP-TMB (Horseradish Peroxidase–3,3“,5,5”-tetramethylbenzidine) assay.[63,64] The hydrogen peroxide photoproduction yield experiment was performed by filling the PEC cell with 14 ml of electrolyte, operating the photoelectrode in potentiostatic mode at OCP dark and illuminating from the electrolyte side with a 110 mW cm^{-2} LED for 60 min. The photocurrent was monitored throughout the whole experiment duration. The total charge is calculated through the integral over the experiment duration. Figure 2b shows the Faraday efficiency determined as the ratio between measured photoelectrons and revealed hydrogen peroxide molecules. For all the three materials a value of just above 3 to 1 is observed. For each H_2O_2 molecule, 2 electrons are needed during the oxygen reduction. Accordingly, ≈2/3 of the photocurrent involves O_2 reduction while 1/3 involves other photoreductions such as HER. This ratio strongly resembles the one initially observed in the photocurrent experiment with and without oxygen (Figure 1b). The electrons that make the ratio exceed the 3-to-1 exact proportion can be reasonably ascribed to the further reduction of the H_2O_2 in solution to H_2O molecules.[65] Figure 2c shows the External Quantum Efficiencies (EQE) measured in the form of electron per incident photon as well as H_2O_2 molecule produced per incident photon for the three materials. As the photoelectrochemical conversion yield is approximately the same for all the polymers, the peroxide generation EQE trend is reflected in the photocurrent EQE trend. As a result, PTB7 outperforms both P3HT and PBDB-T with a roughly fourfold higher photon to peroxide conversion efficiency. We should take into account that the measured photocurrent is only an effective current and does not provide insight on different contributions related to photoreduction, back electron transfer or other electrochemical processes. Similarly, the measured hydrogen peroxide yield must be considered lower limit of the real value as it does not account for H_2O_2 that is further converted to H_2O[65] at the WE, that oxidize the polymer,[37] or that reverts to O_2 in the presence of metallic impurities or catalytic sites.[66] The H_2O_2 photoproduction measured for PTB7, in terms of moles per irradiated mW, is noteworthy also compared with other conjugated polymers that can be found in literature such as TPT polymers[67] or PQTEE-COP.[68]

In the following, we perform microscopic analysis of the different photoelectrodes with the aim to understand why PTB7 is a better oxygen photoreducing polymer. **Figure 3**a compares the surface morphology of the three photoelectrodes as measured by Atomic Force Microscopy. All the films show a low roughness as expected for a spin cast film, with an average R_a of 1.8 nm for P3HT, 1.3 nm for PTB7 and 1.7 nm for PBDB-T. Also, the observed correlation lengths are similar in the three height maps. Therefore, we exclude that increased surface roughness or porosity of the material could be a reason to explain improved performance in PTB7. Another factor possibly governing different photoelectrochemical performance is represented by the different energetic levels in the three materials. By combining KPFM measurements with the photocurrent spectra and literature data, we construct the energy level diagrams of the ITO/p-type polymer junction as described in the following. KPFM maps of the photoelectrode surfaces, obtained in darkness under ambient conditions, are shown in Figure 3b. All the three materials show a narrow distribution of surface potential (V_{RMS} = 24.1±0.2 mV, 19.8±0.1 mV, and 18.9±0.1 mV for P3HT, PBDB-T, and PTB7 respectively) (Figure 3c) and no significant correlation with the height map is present. From the average value of surface potential, we determine the shift in vacuum level across the ITO/semiconductor junction by subtracting the average value measured on the pure ITO surface as reference value. We find shift values V_L of ≈+0.32 V, +0.30 V, and +0.10 V for P3HT, PTB7, and PBDB-T respectively (Figure 3d). The offset between vacuum level and HOMO level is taken for the three polymers from literature as determined by UPS measurements.[46,47] The position of the LUMO-level is then determined by the bandgap as measured with absorption spectroscopy (1.88, 1.60, and 1.8 eV, Figure 3d). Finally, the Fermi-level through the junction is given by the work function of the underlying ITO layer and was determined by KPFM measurements (Work Function = 4.9 eV, Figure 3d). We note that the simplified diagram in Figure 3d does not show different vibronic levels or other higher excited states. Furthermore, it does not show polaronic levels below the LUMO level that accommodate separated excitons and are the states from which free electrons participate in ORR. However, the complete energy level diagram allows us to make two relevant observations for the photoelectrochemical behavior of the p-type polymers: First, materials align energetically in the junction to produce a Fermi-level that shows an offset of 0.53±0.02 eV above the HOMO level in PTB7 and PBDB-T and 0.27±0.02 eV in P3HT (Figure 3d). Accordingly, all three polymers have an excess of positive free carriers. The similar offset energy in PTB7 and PBDB-T points to a polaronic level for hole charges that is similar in energy, while the lower offset in P3HT can be ascribed to the alignment with the bipolaronic level.[69] Second, all the LUMO levels are significantly higher than the typical energy level attributed to the effective one-electron oxygen reduction in water ($O_2/O_2^{-\bullet}$ = 4.1 eV, λ = 0.4 eV[21,70]). Accordingly, also a polaronic level describing free electrons that are energetically below the LUMO, has a good superposition with the oxygen acceptor level making ORR efficient in all three materials. We conclude that the energy-levels difference in the three p-type materials is not enough by itself to explain such a higher efficiency in PTB7 together with such a small difference between P3HT and PBDB-T.

2.2. Structural and Energetic Comparison

As surface morphology and energy levels do not provide significant differences between the three polymer photoelectrodes, we continue our inquiry with investigations of the thin film microstructures with 2D GIWAXS using synchrotron radiation.

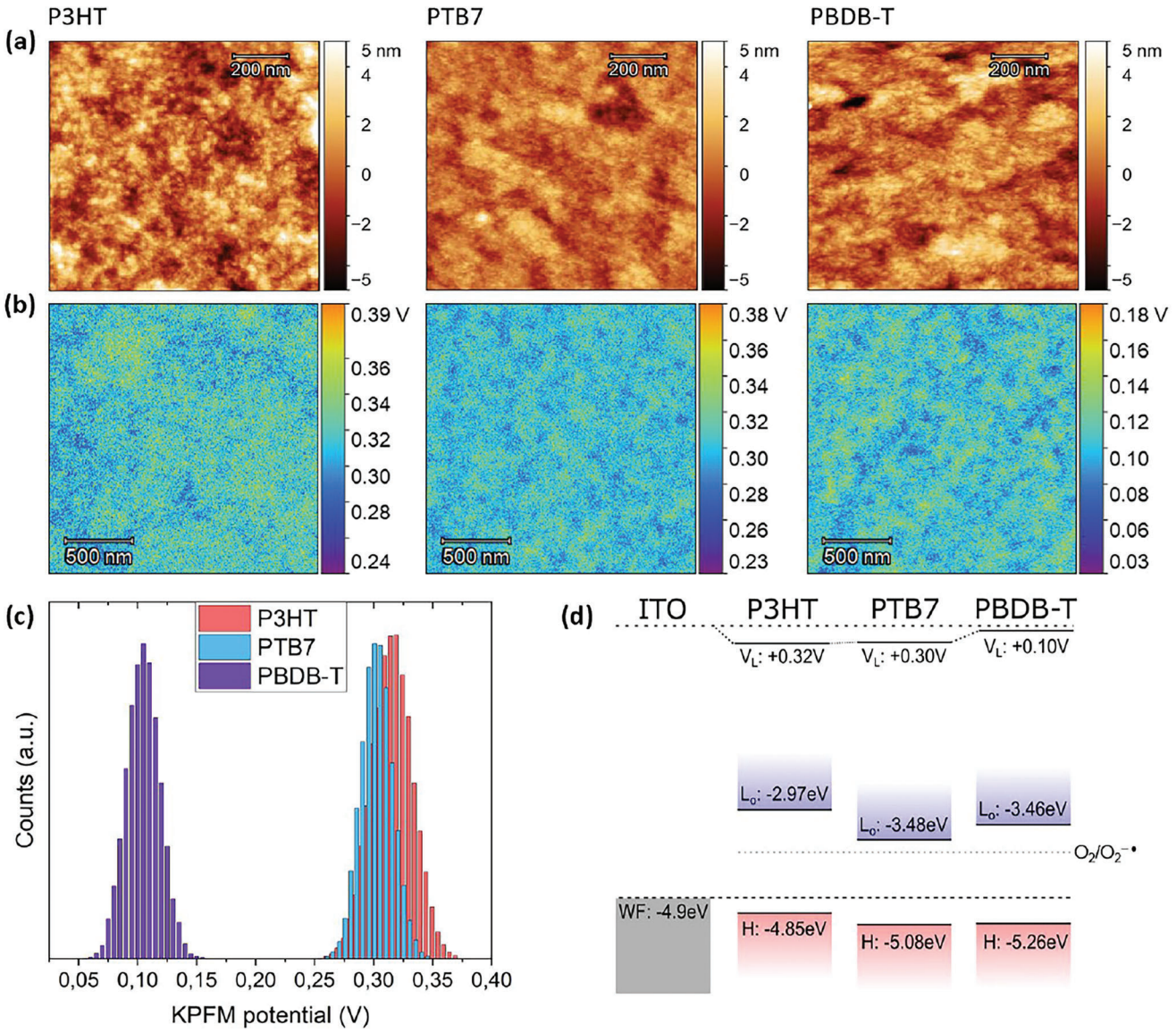

Figure 3. Microstructural and energic investigations on photoelectrodes by Kelvin Probe Force Microscopy (KPFM): a) Height maps show that all polymeric films exhibit low roughness, with an $Rq < 2$ nm. b) KPFM surface potential maps and histograms c) reveal a narrow distribution of potential on all surfaces and a small, but significant offset in PTB7. d) Energy level diagram of the ITO/semiconducting polymer junction for the three different polymers. The levels are determined from the KPFM data, the photocurrent spectra and literature values on HOMO energies referred to the Vacuum level. Polaronic levels below the LUMOs containing free electrons participating in ORR are not shown.

Figure 4 shows the 2D intensity maps and corresponding intensity profiles for the in-plane and out-of-plane directions to extract information about the degree of order and the polymer chain orientation with respect to electrochemical interface. The distinguished patterns show that P3HT is the material with the higher degree of crystallinity, followed by PTB7 and PBDB-T. The preferential orientations are different as well.

The peaks at lower q, between 3 and 12 nm^{-1}, are attributed to the interchain ordering reflection and its harmonics. Reflections at q higher than 15 nm^{-1} are associated with the π-π stacking in the semiconducting polymers. Importantly, the comparison between the GIWAXS in-plane and out-of-plane profiles provides information on the preferential orientation of the π -systems as illustrated in Figure 4c. In P3HT the reflection associated to π-π stacking appears more pronounced in the in-plane direction whereas the one at lower q appears stronger in the out-of-plane direction. This finding points to an "edge-on" configuration in the investigated P3HT photoelectrodes and agrees with typical structures observed in P3HT thin films. In contrast PTB7 shows the opposite behavior of the GIWAXs pattern even though peaks are less pronounced, and the material has an overall lower crystallinity, coherent with a more rigid backbone. Accordingly, PTB7 presents a preferential face-on configuration. Finally, with PBDB-T, the π-π stacking reflections again is clearly more oriented in the vertical direction although it presents a diffraction pattern with edge-on features. Therefore, the film with PBDB-T present

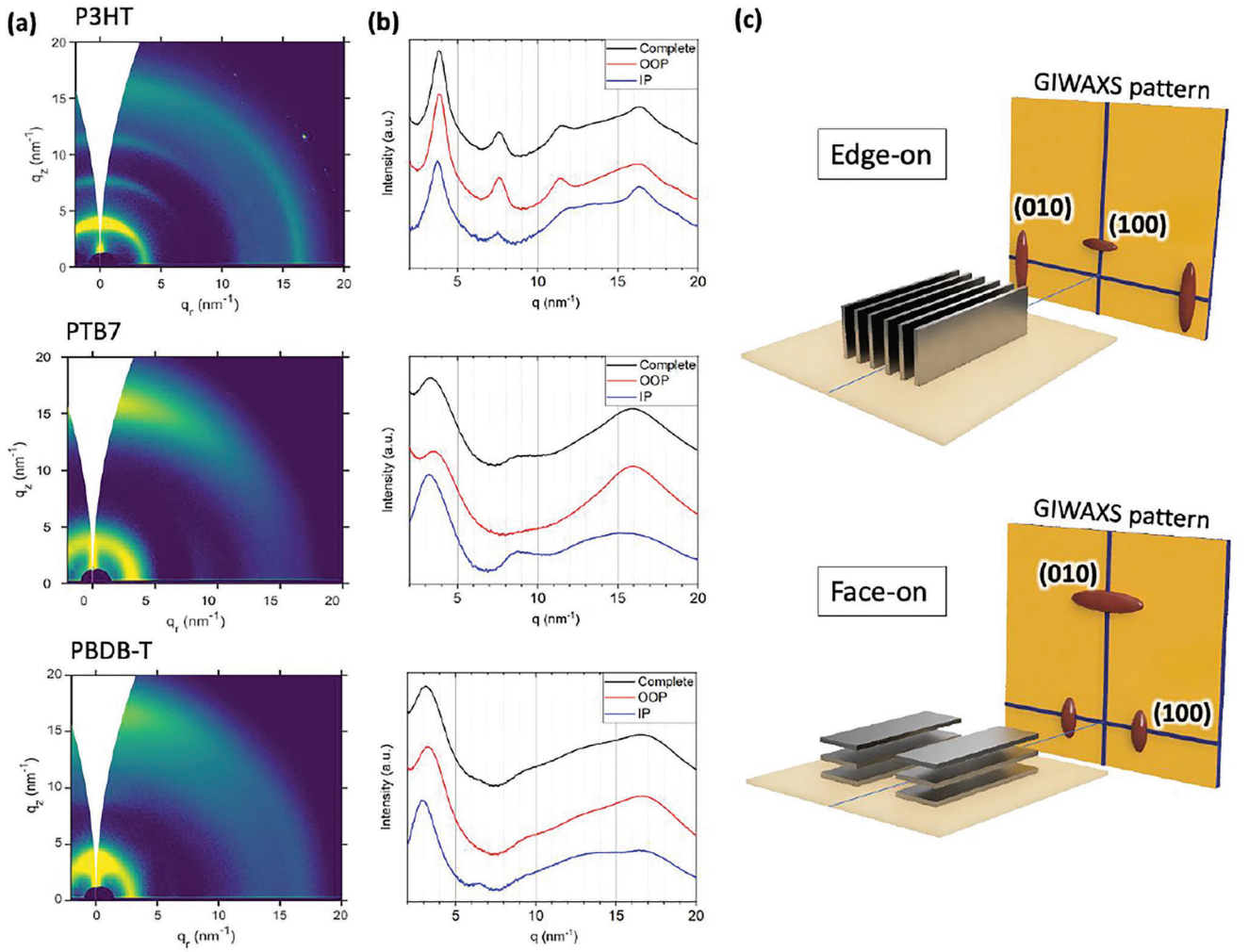

Figure 4. Microstructural investigation of polymer thin films in photoelectrodes with 2D GIWAXS a) and corresponding in-plane (IP) and out-of-plane (OOP) linecuts b). The data shows that P3HT has a higher degree of order, and some oriented crystallites are visible, PTB7 has a mostly an amorphous behavior and a short-range order, and PBDB-T even more. Face-on and edge-on orientations of the polymer chains and their relative GIWAXS pattern are shown in c). We attribute the edge-on configuration to P3HT while PTB7 has a preferential face-on configuration.

both molecular orientations. We propose to relate the characteristic differences in chain orientation to the photoelectrochemical behavior. In the edge-on configuration, as present in P3HT, electron transfer to acceptors beyond the interface must occur across a layer of aliphatic side chains. Such chains have a length of approximately 8 Å and hence they constitute a transport barrier. In contrast, in a face on configuration, crystallites expose the pi-system directly to the aqueous interface and to oxygen acceptor states. Therefore, a faster electron transfer is hypothesized in PTB7 and PBDB-T. We note that in addition to these kinetic arguments on electron transfer, differences in polymer orientation impact also on the surface polarity, dielectric induced stabilization of charge-transfer states[71] and the stabilization of intermediate species in the electrochemical reactions which could further impact on overall efficiency. It should be pointed out that the discussed GIWAXS patterns were taken using an incident angle above the critical angle of the materials, so the scattering comes from the whole thin film material: surface and bulk. If we use an incident angle below that threshold, the scattering information is more surface-sensitive, although not strictly superficial. Nonetheless, the GIWAXS patterns taken at shallow incident angle (≈0.07°) present the same preferential orientation for all the three polymers as in bulk (Figure 4a).

2.3. In–Vitro Efficacy and Biocompatibility Characterization

In the final part of our work, we test the semiconducting polymers at the interface with in–vitro cell cultures. For this purpose, we cultured Human Umbilical Vein Endothelial Cells (HUVECs) on sterilized photoelectrode surfaces. P3HT- and PTB7-cell interfaces were illuminated at a power density of 110 mW cm^{-2} for 3 min with a 530 nm and a 660 nm LEDs, respectively. In the case of PBDB-T, this same illumination protocol caused cell stress and cell detachment (for reasons to be further investigated with an ad hoc study, possibly involving a different chemical/physical interaction with the cell membrane), thus forcing to reduce the illumination intensity to 2 mW cm^{-2}, while keeping 3 min of

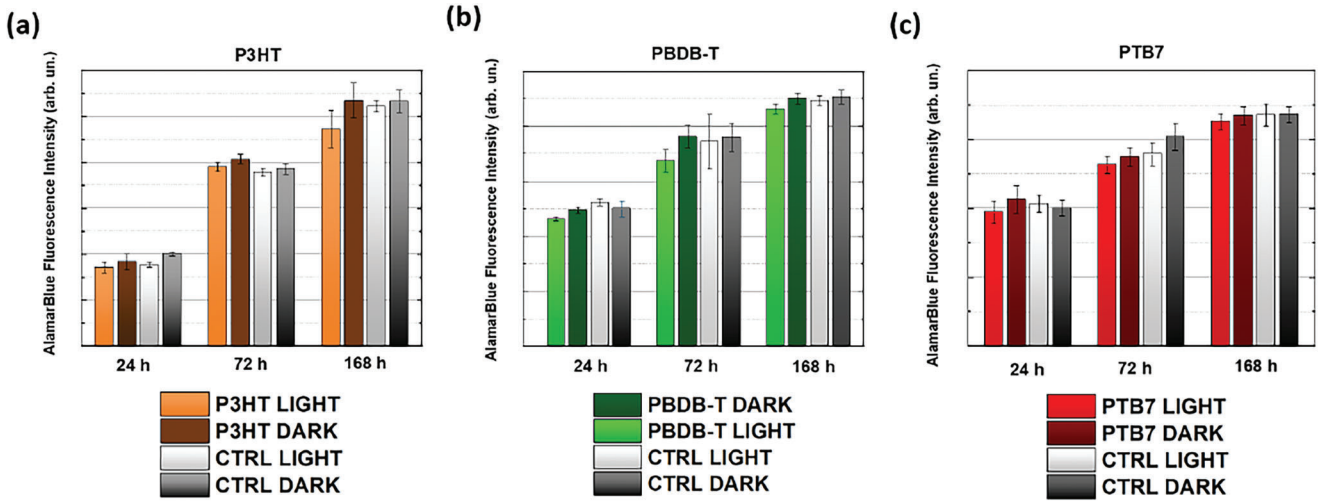

Figure 5. AlamarBlue fluorescence intensity is proportional to the mitochondrial activity inside cells and is representative of cells viability and proliferation. Here we compare P3HT a), PBDB-T b), and PTB7 c) data acquired 24, 48, and 168 h after incubation, over three experiment replicates each.

illumination duration. We then quantified cell viability with the AlamarBlue assay at 24 (immediately after illumination protocol), 72, and 168 h after cell plating, both on polymer and controls substrates, in presence and absence of light stimulus. The AlamarBlue fluorescence signal is an indicator of the metabolic activity inside the cells. In **Figure 5**a clear increase of the fluorescence with time can be observed for all the samples regardless from the presence or absence of the polymer and of the illumination. This means that despite the presence of the polymer photoelectrodes and their generation of ROS, the electrodes fully comply with cell culturing conditions, ROS concentrations fall within a safe, non-toxic range and no detrimental effect is observed on cellular proliferation.

Next, light-induced ROS intracellular production was determined by fluorescent microscopy by incubating HUVECs with the 2",7"-dichlorodihydrofluorescein diacetate (H_2-DCF-DA) probe (**Figure 6**a) and treating them with the same illumination protocol employed in the case of the AlamarBlue assay.[72] As control conditions we tested in parallel ITO samples without polymer and both ITO and ITO/polymer samples kept in dark condition. The results obtained clearly demonstrates that photoexcited PTB7 and PBDB-T are able to increase intracellular ROS concentration as in the prototypical P3HT case (Figure 6b–d). On the contrary, HUVECs treated both with light excitation alone (ITO light) or with the polymers in dark do not show any significant difference as compared to untreated cells (ITO dark, Figure 6b–d).

Overall, these data demonstrate that all the considered polymer photoelectrodes nicely support HUVECs cultures and efficiently drive a sizable enhancement of intracellular ROS species at nontoxic concentration, thus opening the path to the use of semiconducting polymers in the emerging field of "redox-based medicine". While a quantitative correlation between the photoelectrochemical efficiency of the materials and the targeted biological effect on specific cell types in physiological and/or pathological conditions is not possible at this stage, the data presented here certainly account for the possibility to finely tune the optically-driven production of intracellular ROS over a broad range of light intensities and illumination protocols duration.

3. Conclusion

In this work we present a comprehensive characterization of three p-type semiconducting polymers, namely P3HT, PTB7 and PBDB-T, as electrode materials for the photoelectrochemical production of reactive oxygen species (ROS). ROS generation impacts on cellular messaging pathways[41,42] and hence organic semiconductor photoelectrodes enable a new transduction method to impact on cellular phenotype with optical, wireless control. Our study aims to identify the relevant material properties for such an application by comparing different p-type semiconductors. We find that all the three tested materials exhibit photocathodic current generation due to oxygen reduction processes. Interestingly, PTB7 outperformed the other polymers in different examined aspects. Its optical absorbance maximum is centered in the optical transparency window of biological tissue, making it favorable in view of in–vivo applications. In addition, under the employed conditions, PTB7 photocurrent and H_2O_2 generation yields are more than 5 times larger than those shown by the other materials.

As a maximum photocurrent in PTB7 we record 3.04 μA cm^{-2} (at 110 mW cm^{-2}, 660 nm, pH = 7, open circuit potential) which translates into a EQE of $1.7{\cdot}10^{-5}$. We note that higher photocurrents due to ORR can be obtained in thiophene polymers reaching 78 μA cm^{-2} at an illumination of 1SUN when surface roughness is increased and measurement are not performed under open circuit potential.[24] Other thin film compatible materials tested for photoelectrochemical oxygen reduction comprise eumelanin-covered PET films[73] or TMP[74] and have shown a photocurrent densities of 8 μA cm^{-2} and 100 nA cm^{-2} respectively under 1 Sun illumination intensity, but they require a sacrificial reagent, which is not suitable for the physiological environment. In general, quantitative comparisons of different studies on photoelectrochemical hydrogen peroxide generation are difficult to make as the studies aim at different applications and

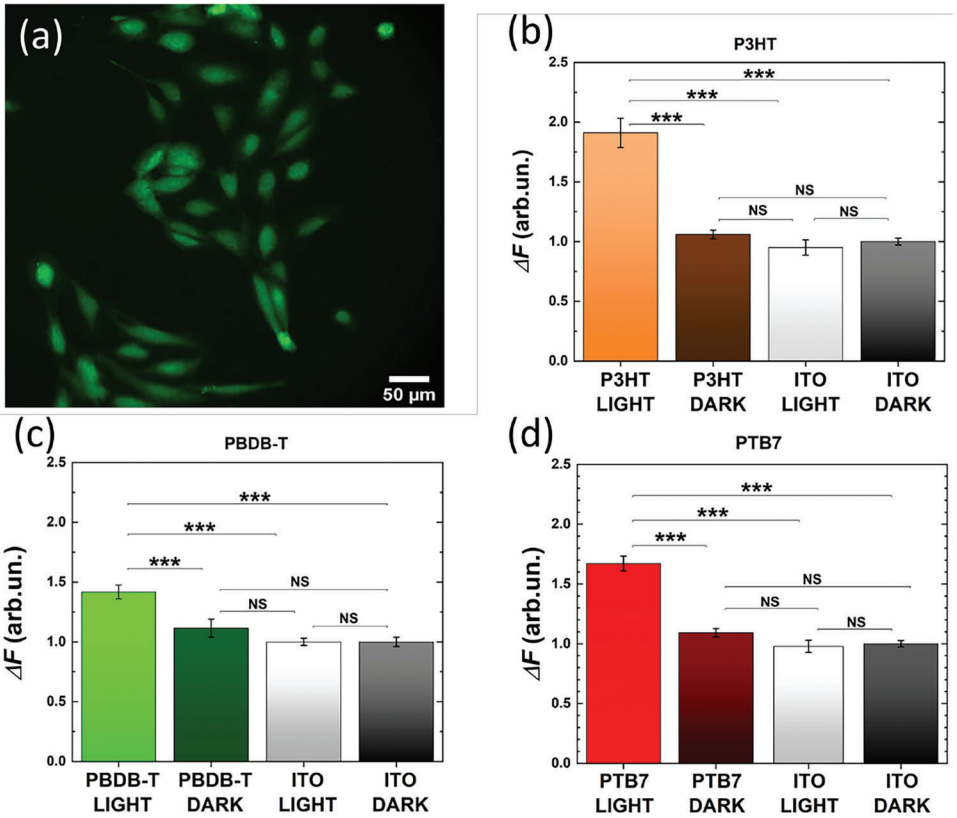

Figure 6. a) Representative fluorescence image depicting HUVECs labelled with the ROS-sensitive DCF-based probe. Average DCF fluorescence intensity (ΔF) s in the case of P3HT(a), PBDB-T(b), PTB7(c), normalized by the value obtained in the control ITO case. DCF excitation/emission wavelengths, 490/520 nm. Photoexcitation conditions: 530 nm @110 mW cm^{-2} for P3HT; 530 nm @2 mW cm^{-2} for PDBD-T; 660 nm @110 mW cm^{-2} for PTB7. Data were compared using the Anova test 2-ways, with Bonferroni correction (0.05 significance level). * p<0.05, ** p<0.01, *** p<0.001. Error bars represent the standard error of the mean.

hence vary measurement conditions.[75] For our case we focus on conditions that mimic the physiological setting of the biomedical device. As this comprises wireless operation, we cannot apply potential to drive photoconversion but we have to measure at open circuit conditions characterizing a floating device.

The higher performance of PTB7 with respect to the other semiconducting polymers is mostly attributed to the face-on configuration of the π-orbital system of the polymer backbone as investigated by GIWAXS. In contrast, P3HT present a preferential Edge-on configuration while PBDB-T present both orientations. These are associated with less efficient electron transfer across the semiconductor/water interface due to barrier properties of aliphatic side chains. The spectroscopic experiments combined with Kelvin-Probe force microscopy allowed us to propose the energy level diagrams for the ITO/semiconductor junction for the three materials. Overall, the three materials show comparable energy levels confirming that the observed differences in photoreduction efficiency are related to proximity effects and kinetic phenomena such as electron transport to acceptor sites. Finally, we demonstrate that all the three polymer photoelectrodes fully support in–vitro HUVECs growth and proliferation. Importantly, they induce significant, physiologically safe levels of intracellular ROS. In conclusion, our results provide comprehensive physico-chemical guidelines for the development of organic photoelectrodes with oxygen reduction properties and provide a useful foundation for their implementation into new photoactive biocompatible devices intended to the ROS-induced modulation of cell physiological activity.

4. Experimental Section

Materials and Sample Preparation: Photoelectrodes were made of a thin polymeric organic semiconductor deposited by spin-coating on ITO coated glass slide (Ossila). The p-type semiconductors rr-P3HT (Ossila), PTB7(Sigma Aldrich) and PBDB-T (Sigma Aldrich) were dissolved in Chlorobenzene at 80 °C at a concentration of 10 mg ml^{-1} and spin-coated at 1000 rpm for 60 s. After deposition the samples were annealed at 100 °C for 10 min. Polymer film thickness of the prepared samples amounted to 50 nm as determined by AFM.

Photocurrent and Photovoltage Spectroscopy, Electrochemical Impedance Measurements: The active surface of the photoelectrode was exposed to PBS electrolyte adjusted in pH to mimic Krebs-Ringer HEPES buffer (0.01 M phosphate buffer, 0.137 M NaCl, pH 7.2 at 25 °C). By mounting the photoelectrode in a dedicated cell only the semiconducting layer was exposed to the electrolyte, while the buried ITO surface and the electrical contacts remain separated via a PDMS O-ring. The cell allows the exposition to the illumination from either the ITO side or the solution side, the latter through a quartz window. In a three-electrode setup the photoelectrode was operated as the working electrode. An Ag|AgCl (3 M KCl) reference electrode was used in combination with a Pt counter elec-

trode. In spectroscopic measurements the monochromatic illumination of the photoelectrode at a defined wavelength was achieved with a Xenon lamp combined with a monochromator (Cornerstone 260). The amplified current or photovoltage signal was filtered and digitized with a lock-in amplifier (Zurich Instruments) connected to the monitoring output of the potentiostat (Metrohm PGSTAT204). The potentiostat was also used for impedance spectroscopy measurements. For transient measurements the monochromated Xenon lamp light was replaced with monochromatic LEDs (Thorlabs M530L4) driven by a source-measure unit (Thorlabs DC2200).

Atomic Force Microscopy and Kelvin-Probe Force Microscopy: Scanning Probe Microscopies were carried out using a Park Instruments NX10 system using NSC36 Cr-Au coated probes (MikroMasch). For KPFM amplitude modulation mode at 17 kHz was used. In order to carry out measurements in illuminated conditions a custom sample holder was built. The illumination was provided by a monochromatic LEDs (Wurth Elektronik) placed beneath the glass surface, driven by a source-measure unit (Keysight B2912A).

Absorption Spectroscopy: Absorption spectra were recorded on a Shimadzu UV-2550 spectrometer equipped with a film adapter, 300–800 nm spectral range, resolution 0.5 nm, 10 nm s^{-1} scan speed.

Grazing Incidence Wide Angle X-ray Spectroscopy: Grazing-Incidence Wide-Angle X-ray Scattering experiments (GIWAXS) were performed at ALBA synchrotron, BL-11 (NCD-SWEET). The X-ray beam wavelength was set at $\lambda = 0.1$ nm. GIWAXS patterns were collected by a LX255-HS 2D (Rayonix) area detector, placed at 21 cm from the sample, using incident angles below 0.15° and exposition times of 1 s.

Hydrogen Peroxide Determination: H_2O_2 concentration was evaluated using Horseradish Peroxidase|3,3′,5,5′-Tetramethylbenzidine (HRP-TMB) assay. Solution used for the assay was freshly prepared by mixing in the following sequence: 10 µL hydrochloric acid solution (HCl in water 1 M) to adjust the pH for the assay, 2 µL horseradish peroxidase solution (HRP in milliQ water, 100 µg mL^{-1}) and 10 µL 3,3',5,5'-tetramethylbenzidine solution (TMB in THF, 10 mg mL^{-1}) in 1.978 mL sample aliquot.

Cell Culture Maintenance: HUVECs were purchased from PromoCell and grown in endothelial cell basal medium (PromoCell), supplemented with Endothelial cell GM 2 supplement pack (PromoCell). Cells were kept in T-75 culture flasks coated with 0.2% gelatin and maintained in incubator at 37 °C in a humidified atmosphere with 5% CO_2. For the experiments, only HUVECs at passage < 7 were employed. After reaching 80–90% of confluence, cells were detached by incubation with 0.5% trypsin-0.2% EDTA (Sigma Aldrich) for 5 min and then plated for experiments.

AlamarBlue Cell Viability Assay: Prior to cell plating, a layer of 1 mg ml^{-1} fibronectin (from bovine plasma, Sigma Aldrich) in phosphate buffer saline (PBS, Sigma Aldrich) was deposited on the surface of the samples and incubated for 30 min, to promote cell adhesion. After removing fibronectin and washing with PBS, cells were plated onto ITO/polymer and bare ITO samples at 20 000 cells/well density. Cell proliferation was evaluated after 24, 48, 168 h after plating in 2 biological replicates. To this aim, AlamarBlue cell reagent was diluted 1:10 in the cell culture medium. In principle, the AlamarBlue molecule, resazurin, was a non-fluorescent molecule that was reduced to a fluorescent compound (resorufin) by the mitochondrial respiratory chain in live cells. In this way, the amount of resorufin produced was directly proportional to the quantity of living cells.

Three aliquots of culture media for each condition were placed in a black 96-well microplate and the fluorescence of the AlamarBlue compound was acquired by a plate reader (TECAN Spark 10 M Plate Reader) with an excitation/emission wavelength of 540/600 nm. The procedure was repeated at each time point, rinsing, and replacing the AlamarBlue compound with fresh medium after each measurement.

Intracellular ROS Detection in HUVECs: 2",7"-dichlorodihydrofluorescein diacetate (H_2DCF-DA, Sigma-Aldrich) was employed for intracellular ROS detection. HUVECs were seeded on polymer and control substrates by following the same procedure employed in the case of the viability assay. The day after plating, the cells were treated continuously for 3 min with Thorlabs LEDs (530 nm @110 mW cm^{-2} for P3HT; 530 nm @2 mW/cm^2 for PDBD-T; 660 nm @110 mW cm^{-2} for PTB7). Immediately after photoexcitation, cell cultures were incubated with 10 µM H_2DCF-DA in KRH for 30 min, at 37 °C with 5% CO_2. After incubation, the fluorescence of the probe was recorded (excitation/emission wavelengths, 490/520 nm, integration time 400 ms, 100 MHz, binning 1) with a 20X objective on an upright fluorescence microscope (Olympus BX63).

Variation of fluorescence intensity was evaluated over regions of interest covering single-cell areas, and reported values represent the average over multiple cells and different samples.

Image processing was carried out with ImageJ and subsequently analyzed with Origin 2020.

Reported results have been mediated over 3 biological replicates, by considering a set of ≈1200 cells and 9 samples for each condition.

Data were compared using the Anova test 2-ways, with Bonferroni correction (0.05 significance level). * p <0.05, ** p <0.01, *** p <0.001. Error bars represent the standard error of the mean.

Supporting Information

Supporting Information is available from the Wiley Online Library or from the author.

Acknowledgements

This research was supported by: EU Horizon 2020 FETOPEN-2018-2020 Programme "LION-HEARTED", grant agreement n. 828984 (L.B., T.C., E.G.F., G.T., D.M., M.R.A.); European Research Council (ERC) under the European Union's Horizon 2020 research and innovation program "LINCE", grant agreement n. 803621 (M.R.A).

Conflict of Interest

The authors declare no conflict of interest.

Data Availability Statement

The data that support the findings of this study are available from the corresponding author upon reasonable request.

Keywords

biocompatible, bioelectronics, HUVECs, organics, photocathodes, photoelectrochemistry, photoelectrodes

Received: March 6, 2023
Revised: May 22, 2023
Published online:

[1] F. Decataldo, T. Cramer, D. Martelli, I. Gualandi, W. S. Korim, S. T. Yao, M. Tessarolo, M. Murgia, E. Scavetta, R. Amici, B. Fraboni, *Sci. Rep.* **2019**, *9*, 10598.
[2] S. T. Keene, V. Gueskine, M. Berggren, G. G. Malliaras, K. Tybrandt, I. Zozoulenko, *Phys. Chem. Chem. Phys.* **2022**, *24*, 19144.
[3] S. Inal, J. Rivnay, A.-O. Suiu, G. G. Malliaras, I. McCulloch, *Acc. Chem. Res.* **2018**, *51*, 1368.
[4] D. Khodagholy, T. Doublet, P. Quilichini, M. Gurfinkel, P. Leleux, A. Ghestem, E. Ismailova, T. Hervé, S. Sanaur, C. Bernard, G. G. Malliaras, *Nat. Commun.* **2013**, *4*, 1575.
[5] M. Berggren, A. Richter-Dahlfors, *Adv. Mater.* **2007**, *19*, 3201.

[6] D. T. Simon, E. O. Gabrielsson, K. Tybrandt, M. Berggren, *Chem. Rev.* **2016**, *116*, 13009.
[7] K. Svennersten, K. C. Larsson, M. Berggren, A. Richter-Dahlfors, *Biochim. Biophys. Acta – Gen. Subj.* **2011**, *1810*, 276.
[8] J. Hopkins, L. Travaglini, A. Lauto, T. Cramer, B. Fraboni, J. Seidel, D. Mawad, *Adv. Mater. Technol.* **2019**, *4*, 1800744.
[9] F. Di Maria, F. Lodola, E. Zucchetti, F. Benfenati, G. Lanzani, *Chem. Soc. Rev.* **2018**, *47*, 4757.
[10] D. Rand, M. Jakešová, G. Lubin, I. Vėbraitė, M. David-Pur, V. Đerek, T. Cramer, N. S. Sariciftci, Y. Hanein, E. D. Głowacki, *Adv. Mater.* **2018**, *30*, 1.
[11] M. J. I. Airaghi Leccardi, N. A. L. Chenais, L. Ferlauto, M. Kawecki, E. G. Zollinger, D. Ghezzi, *Commun. Mater.* **2020**, *1*, 21.
[12] J. F. Maya-Vetencourt, D. Ghezzi, M. R. Antognazza, E. Colombo, M. Mete, P. Feyen, A. Desii, A. Buschiazzo, M. Di Paolo, S. Di Marco, F. Ticconi, L. Emionite, D. Shmal, C. Marini, I. Donelli, G. Freddi, R. MacCarone, S. Bisti, G. Sambuceti, G. Pertile, G. Lanzani, F. Benfenati, *Nat. Mater.* **2017**, *16*, 681.
[13] M. R. Antognazza, M. Di Paolo, D. Ghezzi, M. Mete, S. Di Marco, J. F. Maya-Vetencourt, R. Maccarone, A. Desii, F. Di Fonzo, M. Bramini, A. Russo, L. Laudato, I. Donelli, M. Cilli, G. Freddi, G. Pertile, G. Lanzani, S. Bisti, F. Benfenati, *Adv. Healthcare Mater.* **2016**, *5*, 2271.
[14] M. Silverå Ejneby, M. Jakešová, J. J. Ferrero, L. Migliaccio, I. Sahalianov, Z. Zhao, M. Berggren, D. Khodagholy, V. Đerek, J. N. Gelinas, E. D. Głowacki, *Nat. Biomed. Eng.* **2022**, *6*, 741.
[15] D. Mawad, E. Stewart, D. L. Officer, T. Romeo, P. Wagner, K. Wagner, G. G. Wallace, *Adv. Funct. Mater.* **2012**, *22*, 2692.
[16] I. Abdel Aziz, L. Maver, C. Giannasi, S. Niada, A. T. Brini, M. R. Antognazza, *J. Mater. Chem. C* **2022**, 9823.
[17] G. Onorato, F. Fardella, A. Lewinska, F. Gobbo, G. Tommasini, M. Wnuk, A. Tino, M. Moros, M. R. Antognazza, C. Tortiglione, *Adv. Healthcare Mater.* **2022**, *11*, 2200366.
[18] F. Lodola, V. Rosti, G. Tullii, A. Desii, L. Tapella, P. Catarsi, D. Lim, F. Moccia, M. R. Antognazza, *Sci. Adv.* **2019**, *5*, https://doi.org/10.1126/sciadv.aav4620.
[19] F. Milos, G. Tullii, F. Gobbo, F. Lodola, F. Galeotti, C. Verpelli, D. Mayer, V. Maybeck, A. Offenhäusser, M. R. Antognazza, *ACS Appl. Mater. Interfaces* **2021**, *13*, 23438.
[20] V. Đerek, D. Rand, L. Migliaccio, Y. Hanein, E. D. Głowacki, *Front Bioeng Biotechnol* **2020**, *8*, 1.
[21] T. Paltrinieri, L. Bondi, V. Đerek, B. Fraboni, E. D. Głowacki, T. Cramer, *Adv. Funct. Mater.* **2021**, *2010116*, https://doi.org/10.1002/adfm.202010116.
[22] M. Jakešová, M. Silverå Ejneby, V. Đerek, T. Schmidt, M. Gryszel, J. Brask, R. Schindl, D. T. Simon, M. Berggren, F. Elinder, E. D. Głowacki, *Sci. Adv.* **2019**, *5*, eaav5265.
[23] F. Lodola, N. Martino, G. Tullii, G. Lanzani, M. R. Antognazza, *Sci. Rep.* **2017**, *7*, 8477.
[24] R. Wei, M. Gryszel, L. Migliaccio, E. D. Głowacki, *J. Mater. Chem. C* **2020**, *8*, 10897.
[25] C. Bossio, I. A. Aziz, G. Tullii, E. Zucchetti, D. Debellis, M. Zangoli, F. Di Maria, G. Lanzani, M. R. Antognazza, *Front Bioeng Biotechnol* **2018**, *6*, 1.
[26] J. F. Maya-Vetencourt, G. Manfredi, M. Mete, E. Colombo, M. Bramini, S. Di Marco, D. Shmal, G. Mantero, M. Dipalo, A. Rocchi, M. L. DiFrancesco, E. D. Papaleo, A. Russo, J. Barsotti, C. Eleftheriou, F. Di Maria, V. Cossu, F. Piazza, L. Emionite, F. Ticconi, C. Marini, G. Sambuceti, G. Pertile, G. Lanzani, F. Benfenati, *Nat. Nanotechnol.* **2020**, *15*, 698.
[27] M. R. Antognazza, I. A. Aziz, F. Lodola, *Oxid Med Cell Longev* **2019**, *2019*, https://doi.org/10.1155/2019/2867516.
[28] I. Abdel Aziz, M. Malferrari, F. Roggiani, G. Tullii, S. Rapino, M. R. Antognazza, *iScience* **2020**, *23*, 101091.
[29] E. Mosconi, P. Salvatori, M. I. Saba, A. Mattoni, S. Bellani, F. Bruni, B. S. Gonzalez, M. R. Antognazza, S. Brovelli, G. Lanzani, H. Li, J. L. Brédas, F. De Angelis, *ACS Energy Lett.* **2016**, *1*, 454.
[30] N. Martino, P. Feyen, M. Porro, C. Bossio, E. Zucchetti, D. Ghezzi, F. Benfenati, G. Lanzani, M. R. Antognazza, *Sci. Rep.* **2015**, *5*, 8911.
[31] D. Ghezzi, M. R. Antognazza, M. Dal Maschio, E. Lanzarini, F. Benfenati, G. Lanzani, *Nat. Commun.* **2011**, *2*, https://doi.org/10.1038/ncomms1164.
[32] S. Bellani, D. Fazzi, P. Bruno, E. Giussani, E. V. Canesi, G. Lanzani, M. R. Antognazza, *J. Phys. Chem. C* **2014**, *118*, 6291.
[33] F. Benfenati, G. Lanzani, *Nat. Nanotechnol.* **2021**, *16*, 1333.
[34] G. Chiaravalli, G. Manfredi, R. Sacco, G. Lanzani, *ACS Appl. Mater. Interfaces* **2021**, *13*, 36595.
[35] A. Giovannitti, R. B. Rashid, Q. Thiburce, B. D. Paulsen, C. Cendra, K. Thorley, D. Moia, J. T. Mefford, D. Hanifi, D. Weiyuan, M. Moser, A. Salleo, J. Nelson, I. McCulloch, J. Rivnay, *Adv. Mater.* **2020**, *32*, 1908047.
[36] E. Mitraka, M. Gryszel, M. Vagin, M. J. Jafari, A. Singh, M. Warczak, M. Mitrakas, M. Berggren, T. Ederth, I. Zozoulenko, X. Crispin, E. D. Głowacki, *Adv Sustain Syst* **2019**, *3*, 1.
[37] M. Gryszel, M. Sytnyk, M. Jakešová, G. Romanazzi, R. Gabrielsson, W. Heiss, E. D. Głowacki, *ACS Appl. Mater. Interfaces* **2018**, *10*, 13253.
[38] G. M. Suppes, P. J. Fortin, S. Holdcroft, *J. Electrochem. Soc.* **2015**, *162*, H551.
[39] M. Gryszel, E. D. Głowacki, *Chem. Commun.* **2020**, *56*, 1705.
[40] I. Bargigia, E. Zucchetti, A. R. S. Kandada, M. Moreira, C. Bossio, W. P. D. Wong, P. B. Miranda, P. Decuzzi, C. Soci, C. D'Andrea, G. Lanzani, *ChemBioChem* **2019**, *20*, 532.
[41] E. Panieri, M. M. Santoro, *Cell. Mol. Life Sci.* **2015**, *72*, 3281.
[42] H. Sies, D. P. Jones, *Nat. Rev. Mol. Cell Biol.* **2020**, *21*, 363.
[43] H. Sies, *Antioxidants* **2020**, *9*, 852.
[44] L. Zhang, X. Wang, R. Cueto, C. Effi, Y. Zhang, H. Tan, X. Qin, Y. Ji, X. Yang, H. Wang, *Redox Biol.* **2019**, *26*, 101284.
[45] D. Andrienko, M. Brinkmann, K. Daoulas, D. Djurado, L. Hartmann, N. Kayunkid, S. Ludwigs, C. K. Luscombe, A. J. Moulé, D. Neher, C. Poelking, P. Sista, K. Tremel, A. Troisi, S. T. Turner, J. Zaumseil, *P3HT Revisited – from Molecular Scale to Solar Cell Devices*, Springer, Hamburg **2014**.
[46] Y. Xue, F. Yang, J. Yuan, Y. Zhang, M. Gu, Y. Xu, X. Ling, Y. Wang, F. Li, T. Zhai, J. Li, C. Cui, Y. Chen, W. Ma, *ACS Energy Lett.* **2019**, 2850.
[47] Y. Yi, J. E. Lyon, M. M. Beerbom, R. Schlaf, *J. Appl. Phys.* **2006**, *100*, 093719.
[48] U. Aygül, H. Peisert, J. Frisch, A. Vollmer, N. Koch, T. Chassé, *ChemPhysChem* **2011**, *12*, 2345.
[49] C. Wang, W. Zhang, X. Meng, J. Bergqvist, X. Liu, Z. Genene, X. Xu, A. Yartsev, O. Inganäs, W. Ma, E. Wang, M. Fahlman, *Adv. Energy Mater.* **2017**, *7*, 1.
[50] F. Bencheikh, D. Duché, C. M. Ruiz, J. J. Simon, L. Escoubas, *J. Phys. Chem. C* **2015**, *119*, 24643.
[51] S. Dayal, N. Kopidakis, D. C. Olson, D. S. Ginley, G. Rumbles, *Nano Lett.* **2010**, *10*, 239.
[52] T. Umeyama, K. Igarashi, D. Sasada, Y. Tamai, K. Ishida, T. Koganezawa, S. Ohtani, K. Tanaka, H. Ohkita, H. Imahori, *Chem. Sci.* **2020**, *11*, 3250.
[53] H. Hintz, H. J. Egelhaaf, L. Lüer, J. Hauch, H. Peisert, T. Chassé, *Chem. Mater.* **2011**, *23*, 145.
[54] M. Brinkmann, *J. Polym. Sci., Part B: Polym. Phys.* **2011**, *49*, 1218.
[55] A. T. Kleinschmidt, S. E. Root, D. J. Lipomi, *J. Mater. Chem. A* **2017**, *5*, 11396.
[56] S. Brixi, O. A. Melville, N. T. Boileau, B. H. Lessard, *J. Mater. Chem. C* **2018**, *6*, 11972.
[57] Z. Zheng, H. Yao, L. Ye, Y. Xu, S. Zhang, J. Hou, *Mater. Today* **2020**, *35*, 115.

[58] L. Lu, L. Yu, *Adv. Mater.* **2014**, *26*, 4413.
[59] S. Bellani, M. R. Antognazza, F. Bonaccorso, *Adv. Mater.* **2019**, *31*, 1.
[60] A. M. Smith, M. C. Mancini, S. Nie, *Nat. Nanotechnol.* **2009**, *4*, 710.
[61] J. Guo, H. Ohkita, H. Benten, S. Ito, *J. Am. Chem. Soc.* **2009**, *131*, 16869.
[62] Q. Zhou, G. Shi, *J. Am. Chem. Soc.* **2016**, *138*, 2868.
[63] P. D. Josephy, T. Eling, R. P. Mason, *J. Biol. Chem.* **1982**, *257*, 3669.
[64] S. G. Rhee, T. S. Chang, W. Jeong, D. Kang, *Mol. Cells* **2010**, *29*, 539.
[65] E. Mitraka, M. Gryszel, M. Vagin, M. J. Jafari, A. Singh, M. Warczak, M. Mitrakas, M. Berggren, T. Ederth, I. Zozoulenko, X. Crispin, E. D. Głowacki, *Adv Sustain Syst* **2019**, *3*, 1800110.
[66] B. R. Petigara, N. V. Blough, A. C. Mignerey, *Environ. Sci. Technol.* **2002**, *36*, 639.
[67] Y. Sun, L. Han, P. Strasser, *Chem. Soc. Rev.* **2020**, *49*, 6605.
[68] X. Xu, H. Zhong, W. Huang, Y. Sui, R. Sa, W. Chen, G. Zhou, X. Li, D. Li, M. Wen, B. Jiang, *Chem. Eng. Journal* **2023**, *454*, 139929.
[69] C. Enengl, S. Enengl, S. Pluczyk, M. Havlicek, M. Lapkowski, H. Neugebauer, E. Ehrenfreund, *ChemPhysChem* **2016**, *17*, 3830.
[70] R. Memming, *Semiconductor Electrochemistry* **2015**.
[71] Z. Hu, A. P. Willard, R. J. Ono, C. W. Bielawski, P. J. Rossky, D. A. Vanden Bout, *Nat. Comm.* **2015**, *6*, 8246.
[72] D. Wu, P. Yotnda, *J Vis Exp* **2011**, *2*.
[73] L. Migliaccio, M. Gryszel, V. Đerek, A. Pezzella, E. D. Głowacki, *Mater. Horiz.* **2018**, *5*, 984.
[74] H. Yan, Y. Deng, M. Shen, Y.-X. Ye, F. Zhu, X. Yang, G. Ouyang, *Appl Catal B* **2022**, *314*, 121488.
[75] K. Oka, B. Winther-Jensen, H. Nishide, *Adv. Energy Mater.* **2021**, *11*, 43.